Low-Dimensional Hyperthin FeS_2 Nanostructures for Efficient and Stable Hydrogen Evolution Electrocatalysis

Daniel Jasion[1]†, Joseph M. Barforoush[2,3]†, Shenqiang Ren[1,3,4], and Kevin C. Leonard[2,3]**

[1]Department of Chemistry, University of Kansas, Lawrence, KS 66045, United States.

[2]Department of Chemical Engineering, University of Kansas, Lawrence, KS 66045, United States.

[3]Center for Environmentally Beneficial Catalysis, University of Kansas, Lawrence, KS 66045, United States.

[4] Department of Mechanical Engineering, Temple University, Philadelphia, PA 19122

KEYWORDS: Electrocatalysis, Hydrogen Evolution, Water Splitting, FeS_2

ABSTRACT: We report a scalable, solution-processing method for synthesizing low-dimensional hyperthin FeS_2 nanostructures, and show that 2D FeS_2 disc nanostructures are an efficient and stable hydrogen evolution electrocatalyst. By changing the Fe:S ratio in the precursor solution, we were able to preferentially synthesize either 1D wire or 2D disc nanostructures. The 2D FeS_2 disc structure has the highest electrocatalytic activity for the hydrogen evolution reaction, comparable to platinum in neutral pH conditions. The ability of the FeS_2 nanostructures to generate hydrogen was confirmed by scanning electrochemical microscopy, and the 2D disc nanostructures were able to generate hydrogen for over 125 hours.

MAIN TEXT:

A key green energy initiative is the discovery of efficient, stable, and elemental abundant electrocatalysts for the water splitting reactions, i.e. the hydrogen evolution reaction (HER) and the oxygen evolution reaction (OER).[1-3] Water splitting with HER and OER electrocatalysts play a vital role in converting solar energy into chemical energy via artificial photosynthesis, and also provides a pathway to use water (as opposed to natural gas) as a feedstock for hydrogen production.[4-6] Nanostructured transition-metal chalcogenides have previously been studied as HER electrocatalysts.[7-12] In particular, two-dimensional (2D) MoS_2 nanosheets are effective HER catalysts under acidic conditions,[9,13] and it has been discussed that the HER activity correlates with number of edge sites on the MoS_2 and/or the hopping efficiency of electrons in the vertical direction.[14-15] While other transition-metal chalcogenides have also been studied as HER catalysts (e.g. WS_2, NiS_2, CoS_2, $NiSe_2$, and $CoSe_2$),[8,16] there have been only limited reports on the catalytic activity of FeS_2,[8,17] and none have shown high efficiency for FeS_2. In order to improve the electrocataltyic activity of earth-abundant FeS_2, we report a novel synthesis technique for the creation of hyperthin 1D and 2D FeS_2 nanostructures, which we term “wires” and “discs”

respectively. We show that the 2D FeS_2 disc nanostructure has high catalytic activity for the HER, very similar to Pt, and is stable in neutral pH conditions.

Many different nanostructured morphologies of iron sulfides have previously been identified.[18-20] However, reports of low dimensional iron sulfide nanostructures with atomic layer thickness have been rare and were typically seen as an intermediate.[21-23] Previous, methods for producing iron sulfides with atomic layer thickness have relied on chemical vapor deposition (CVD), electrodeposition, techniques requiring high temperature sulfurization, and/or a brute force cleavage.[24-27]

Here we utilize a solution hot-injection method, analogous to a previously reported iron sulfide synthesis,[23] to create unique hyperthin iron sulfide nanostructures with atomic layer thickness. In the first step of the synthesis, an octadecylamine (ODA) ligand was added to a Fe^{2+} solution, which formed ~3-5 nm iron nanoparticles as seen in the transmission electron microscopy, TEM, images (Figure 1a,e). The ODA ligand acts as both a reducing agent for the Fe^{2+} (Equation 1) and as a capping layer on the subsequent nanocrystal formation. Next, upon injection of sulfur, the iron seed particles oxidize to form Fe^{2+} and S_x^{2-} moieties (Equation 2) and these species form the FeS_2 nanostructures via Equations 3 and 4.

$$Fe^{2+} + 2e^- \xrightarrow{L} Fe^0 \quad (1)$$

$$Fe^0 + S_x \rightarrow Fe^{2+} + S_x^{2-} \quad (2)$$

$$Fe^{2+} + S_x^{2-} \rightarrow FeS + S_{x-1} \quad (3)$$

$$FeS + S_x^{2-} \rightarrow FeS_2 + S_{x-1}^{2-} \quad (4)$$

It was found that low dimensional structural formation could be tuned through adjustments of the initial sulfur concentration with two primary low dimensional FeS_2 nanostructures being observed. Changing the Fe:S ratio present in the precursor solutions formed

either distinct wire or disc nanostructures as seen in Figure 1. We determined that a 1:6 Fe:S ratio yields wires (Figure 1b,f) uniformly separated by a tightly packed layer of ligand (Figure 1d) with a spacing of approximately 2.7 nm. Increasing the Fe:S ratio to 1:24 results in the formation of discs (Figure 1c,g) which appear in a stack of thin sheets also separated by a ligand layer.

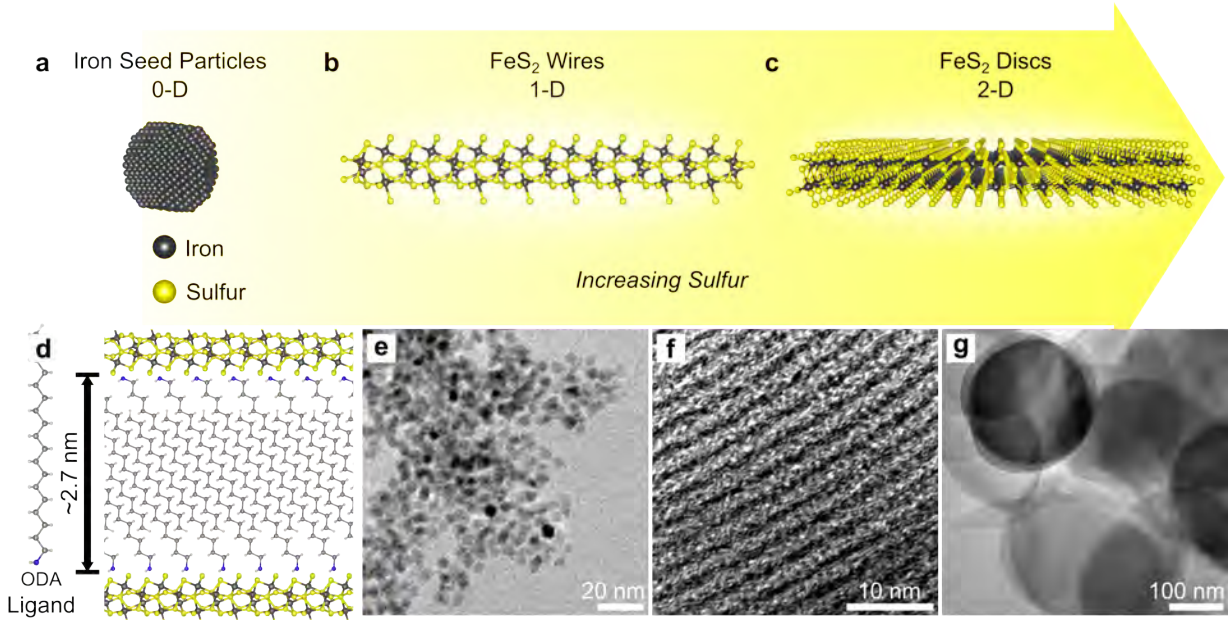

Figure 1. Schematic representation and TEM images of the 1D and 2D FeS_2 structure formation. (a) and (e) are the Fe^0 nanoparticles that are formed in the absence of sulfur. (b) and (f) are the FeS_2 wires formed from 1:6 Fe:S precursor solution. (c) and (g) are the FeS_2 discs formed in the 1:24 Fe:S precursor. (d) is the ~2.7 nm wide ligand interstitial layer that separates both wires and discs to form their respective bulk structures.

The kinetics of the wire and disc reactions were tracked through (1) time dependent growth patterns monitored by TEM (Figure 2); (2) energy-dispersive X-ray spectroscopy (EDS) measurements (Figure 2i), which monitored the rate at which the Fe:S stoichiometry changed; and (3) UV-Vis-IR spectra (Figure S1) which showed the changes in the relative peak heights of

the FeS_2 characteristic set of absorbance peaks with respect to reaction time. The transition to FeS_2 was kinetically different between the wire and disc structures. The wire reaction (Figure 2a-c) occurred relatively slowly, with the iron seed particles still present for several minutes into the reaction. Examination of the disc reaction (Figure 2e-g) revealed faster kinetics with initial disc formation occurring within seconds of the injection and the seed particles being consumed minutes earlier than the wires. The EDS measurements correlate well with both the TEM and absorbance data. The wires reached the desired 1:2 stoichiometry after 30-60 minutes and maintained that stoichiometry for the duration of the reaction. The 1:24 Fe:S precursor ratio (discs) showed a faster conversion. Within 30 seconds, disc formations were observed, and 10 minutes into the reaction the discs reached a 1:2 Fe:S ratio. The scanning electron microscopy (SEM) characterization of the final wire structure (Figure 2d) showed the bulk wires forming long bundled strands with lengths well over a micron which come together to form a porous sponge-like structure held together by ligand-ligand interactions. The SEM image of the final disc structure (Figure 2h) also showed the stacking of discs to form larger structures with a range of diameters from 300 to 800 nm that most likely are connected by ligand-ligand interactions.

Raman spectroscopy was used to further elucidate structure and phase identification (Figure 2j). Both the wire and disc structures share a characteristic set of Raman peaks at 291 and 358 cm^{-1}.[25] The combination of the EDS data and ordered nanostructures within TEM images led to the conclusion that these peaks correspond to an ordered FeS_2 structure. The thinness of these materials may not allow for the more typical Raman active modes[28-29] of the usual FeS_2 phases (e.g. pyrite, marcasite) nor of the other typical $Fe_{1-x}S$ phases. X-ray diffraction (XRD, Figure S2) confirmed the presence of Fe nanoparticles in the early stages but exhibited no

discernable phase in the final products, potentially due to the thinness of the material leading to insufficient scattering volume.

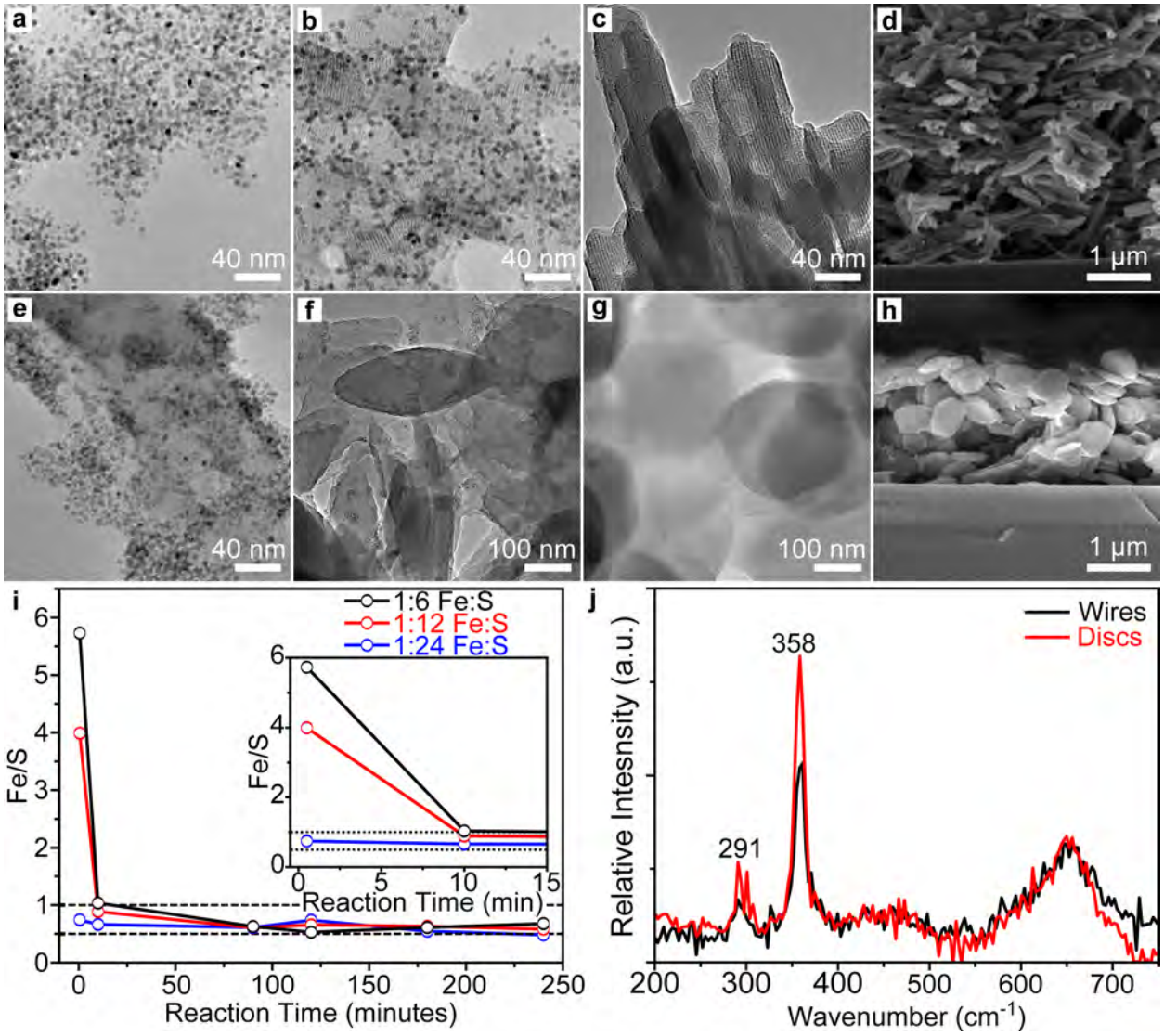

Figure 2. Time Dependent TEM characterization is shown for the wires (a-c) and discs (e-g) taken at 0.5, 5, and 240 minutes, respectively. SEM characterization of the final wire (d) and disc (h) formations cast on Si substrates. Time dependent EDS measurements (i) are shown with the inset focusing on the first 15 minutes of the reaction. The plot of the Raman spectroscopy data (j) is to establish phase identification.

The HER electrocatalytic activity of the nanostructured FeS_2 (drop-casted on a glassy carbon electrode) was measured via linear sweep voltammetry (LSV) at 1 mV/s in 0.1 M pH 7 phosphate buffer solution (PBS) (see Supporting Information for experimental details). Figure 3a (solid lines) shows the capacitance and i-R corrected LSVs for the champion FeS_2 1D wires, 2D discs, 3D cubes (TEM for the 3D FeS_2 cubes shown in Figure S3b) along with a blank glassy carbon electrode and Pt electrode. By synthesizing 2D FeS_2 nanostructures, we were able to shift the onset potential to very near the thermodynamic potential for hydrogen evolution (0 V vs RHE) indicative of exceptionally high electrocatalytic activity. In fact, these novel 2D FeS_2 nanostructures have an overpotential less than 50 mV larger than that of Pt. Triplicates of the LSV experiments obtained from separate batches of the FeS_2 1D wires, 2D discs, and 3D cubes (Figure S3a) show good reproducibility between samples with variances attributed to variability in electrode fabrication.

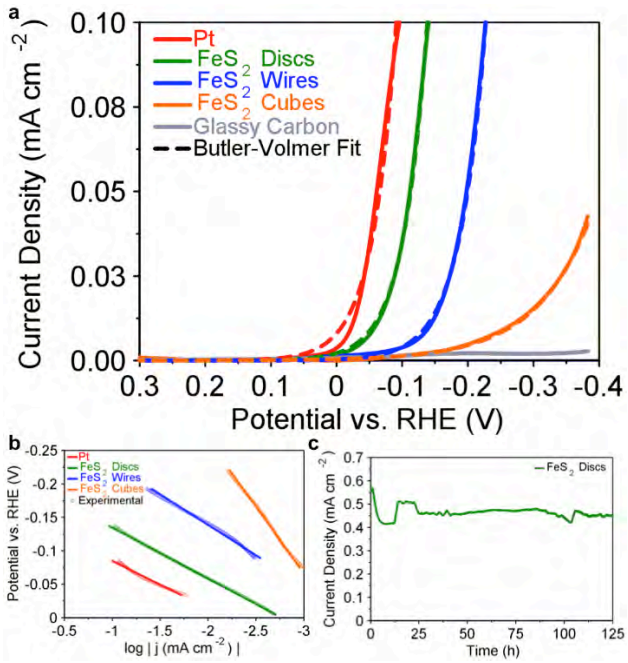

Figure 3. Electrochemical characterization of FeS_2 discs, wires, and cubes in 0.1 M pH 7 phosphate buffer solution (PBS) for the hydrogen evolution reaction. (a) Experimental linear sweep voltammograms at 1 mV/s (solid lines) for the champion FeS_2 discs, wires, and cubes coated on glassy carbon along with a bare Pt electrode and a bare glassy carbon electrode. Also shown are the corresponding best-fit single-electron Butler-Volmer equations (dashed lines) for each electrode. (b) Tafel plot showing the experimental data in the Tafel region (circle markers) with the corresponding Tafel slopes (solid lines) for Pt, FeS_2 discs, wires, and cubes. (c) Current density vs. time profile for a 125-hour constant potential (-0.14 V vs. RHE) stability test for the FeS_2 discs under continuous stirring.

To quantify the electrocatalytic activity, the pseudo-steady state measurements were fit to the single-electron transfer Butler-Volmer equation (dashed lines, Figure 3a) assuming no mass-transfer effects (Equation S1). This allowed for accurate exchange current densities and transfer coefficients to be obtained for each structure. It should be noted that at this scan rate, the mass-

transfer limited regime is reached at much lower currents than typically seen at faster scan rates (Figure S4) due to limited transient effects and lower concentration gradients near the electrode surface. From the Butler-Volmer equation, the exchange current density, which is a measure of kinetics for the hydrogen evolution reaction,[30] for the FeS_2 discs, wires, and cubes were determined to be 2.2, 0.32, and 0.41 μA cm^{-2}, respectively, while Pt had an exchange current density of 8.0 μA cm^{-2}. This shows that only the 2D FeS_2 disc nanostructures had an exchange current density on the same order of magnitude as Pt. A secondary calculation of the exchange current densities and transfer coefficients were obtained from Tafel analysis (Figure 3b). The Tafel plot yielded exchange current densities of 6.3, 1.7, 0.30, and 0.47 μA cm^{-2} for Pt and the FeS_2 discs, wires, and cubes, respectively. All of the exchange current densities as calculated via the Tafel plot are within 25% of those values calculated with the Bulter-Volmer equation.

The transfer coefficients, α, obtained from the Butler-Volmer equation were determined to be 0.71, 0.71, 0.65, and 0.31 for Pt and the FeS_2 discs, wires, and cubes, respectively. Tafel slopes of Pt and the FeS_2 discs, wires, and cubes were 70.53, 76.05, 91.38, and 200.4 mV per decade, respectively, which correlates to transfer coefficients of 0.82, 0.76, 0.64, and 0.29. The transfer coefficient is a measure of the symmetry of the energy barrier going from the oxidized to the reduced species.[30] Similar transfer coefficients and Tafel slopes between the 2D FeS_2 disc structure and Pt suggests that the 2D FeS_2 structure has a Pt-like HER mechanism in neutral pH.

To determine the stability of the FeS_2 discs, a constant potential of -0.14 V vs RHE was applied for over 125 hours in 0.1 M pH 7 PBS while vigorously stirring, and the reduction current was measured as a function of time. Figure 3c shows that the reduction current did not change significantly over the 125-hour experiment. This suggests that, by maintaining reducing conditions (i.e. negative potentials) sufficient to evolve hydrogen, the FeS_2 discs catalyst is stable

for generating hydrogen from water under neutral pH conditions. The turnover frequency (TOF) was calculated from Equation S2 using the data presented in Figure 3c and the electrochemical surface area, which was calculated from double-layer capacitance measurements. The TOFs of the FeS_2 discs and the Pt electrode were determined to be 128 electrons h^{-1} and 644 electrons h^{-1} under the same conditions (Figure S5) with the FeS_2 discs having more than double the electrochemical surface area than the Pt electrode.

To verify that hydrogen was evolving from the surface of the 2D FeS_2 discs, an HER electrochemical reactivity map was obtained via scanning electrochemical microscopy (SECM, Figure 4). SECM is a powerful technique for imaging the reactivity of electrocatalytic surfaces and for studying electrochemical reactions.[31-33] Figure 4a shows the schematic for obtaining a hydrogen evolution electrochemical reactivity map. Here the catalytic electrode was held at a negative potential sufficient to evolve hydrogen and a 200 μm Pt SECM tip electrode was held at a positive potential sufficient to oxidize any hydrogen present in solution. The SECM tip electrode was placed c.a. 100 μm above the catalyst electrode and was scanned across the catalyst surface while the tip current was recorded as a function of tip position. Areas where hydrogen is being generated by the catalyst electrode will produce an oxidation current on the SECM tip electrode at that position.

HER electrochemical reactivity maps were obtained on the Pt electrode, the 2D FeS_2 discs coated on glassy carbon, and a bare glassy carbon electrode (Figures 4b-d). Both the Pt (Figure 4c) and the 2D FeS_2 discs-coated electrode (Figure 4d) shows oxidation currents (reds, yellows, and greens) on the SECM tip electrode, indicative of hydrogen existing in solution over each electrode. For comparison, Figure 4b shows no hydrogen in solution for the bare glassy carbon electrode operated at the same potential at which Figure 4c was generated. Thus, via

these SECM electrochemical reactivity maps, we can conclude that the FeS_2 discs catalyst is indeed generating hydrogen gas.

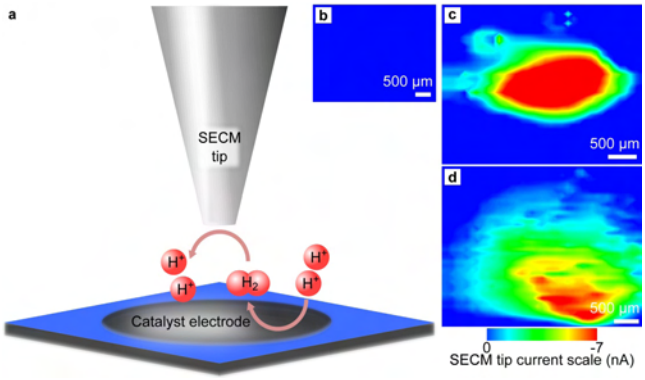

Figure 4. Hydrogen evolution electrochemical reactivity maps obtained via scanning electrochemical microscopy (SECM). (a) Schematic of the SECM experiment showing hydrogen collection on the SECM tip electrode. (b) The reactivity map for bare glassy carbon electrode. (c) and (d) Electrochemical reactivity maps for the HER on Pt and FeS_2 discs on glassy carbon, respectively.

In summary, we report a novel synthesis method to create 2D FeS_2 nanostructures, which significantly improves the electrocatalytic performance of earth-abundant FeS_2 for the HER. It was found that the morphology and stoichiometry of the FeS_2 could be tuned by the initial sulfur concentration. The 1D FeS_2 wires and the 2D FeS_2 discs showed higher electrocatalytic activity compared to the conventional 3D FeS_2 cubes for the HER under neutral pH conditions. In fact, the 2D FeS_2 materials displayed excellent electrochemical activity – similar to platinum – with high exchange current densities and an onset potential for hydrogen evolution near the thermodynamic potential. The 2D FeS_2 discs also proved to be remarkably stable demonstrating the ability to generate hydrogen for over 125 hours when under reducing conditions. Using SECM, we verified that hydrogen was being generated from both the Pt and FeS_2 discs electrodes, but not from a bare glassy carbon electrode.

ASSOCIATED CONTENT

Supporting Information. FeS_2 nanoparticle synthesis and characterization, experimental methods, Equation S1-S2 and Figures S1-5. This material is available free of charge via the Internet at http://pubs.acs.org.

AUTHOR INFORMATION

Corresponding Author

*kcleonard@ku.edu *shenqiang.ren@temple.edu

Present Addresses

†If an author's address is different than the one given in the affiliation line, this information may be included here.

Author Contributions

†These authors contributed equally to this work

Funding Sources

S.R. thanks the financial support from the U.S. National Science Foundation (NSF) under Award No: NSF-DMR-1451326 for nanocrystal synthesis, and Army Research Office-Young Investigator Award (W911NF-14-1-0443) for functional material design and self-assembly. K.C.L thanks the financial support from KU's College of Engineering and Department of Chemical and Petroleum Engineering.

Notes

Any additional relevant notes should be placed here.

ACKNOWLEDGMENT

D.J. would like to acknowledge the Microscopy and Analytical Imaging Laboratory (MAI) lab at KU for help in TEM and SEM characterization as well as Dr. Victor Day for help with XRD characterization.

REFERENCES

1. Kanan, M. W.; Nocera, D. G. *Science* **2008,** *321*, 1072-1075.

2. McKone, J. R.; Warren, E. L.; Bierman, M. J.; Boettcher, S. W.; Brunschwig, B. S.; Lewis, N. S.; Gray, H. B. *Energy Environ. Sci.* **2011,** *4*, 3573-3583.

3. Leonard, K. C.; Bard, A. J. *J. Am. Chem. Soc.* **2013,** *135*, 15885-15889.

4. McKone, J. R.; Lewis, N. S.; Gray, H. B. *Chem. Mater.* **2014,** *26*, 407-414.

5. Lewis, N. S.; Nocera, D. G. *Proc. Natl. Acad. Sci. U.S.A.* **2006,** *103*, 15729-15735.

6. Gray, H. B. *Nat. Chem.* **2009,** *1*, 7-7.

7. Yang, J.; Shin, H. S. *J. Mater. Chem. A* **2014,** *2*, 5979-5985.

8. Kong, D. S.; Cha, J. J.; Wang, H. T.; Lee, H. R.; Cui, Y. *Energy Environ. Sci.* **2013,** *6*, 3553-3558.

9. Lukowski, M. A.; Daniel, A. S.; Meng, F.; Forticaux, A.; Li, L. S.; Jin, S. *J. Am. Chem. Soc.* **2013,** *135*, 10274-10277.

10. Di Giovanni, C.; Wang, W.-A.; Nowak, S.; Grenèche, J.-M.; Lecoq, H.; Mouton, L.; Giraud, M.; Tard, C. *ACS Catal.* **2014,** *4*, 681-687.

11. Peng, Z.; Jia, D.; Al-Enizi, A. M.; Elzatahry, A. A.; Zheng, G. *Adv. Energy Mater.* **2015,** *5*.

12. Sun, Y.; Liu, C.; Grauer, D. C.; Yano, J.; Long, J. R.; Yang, P.; Chang, C. J. *J. Am. Chem. Soc.* **2013,** *135*, 17699-17702.

13. Li, Y. G.; Wang, H. L.; Xie, L. M.; Liang, Y. Y.; Hong, G. S.; Dai, H. J. *J. Am. Chem. Soc.* **2011,** *133*, 7296-7299.

14. Jaramillo, T. F.; Jorgensen, K. P.; Bonde, J.; Nielsen, J. H.; Horch, S.; Chorkendorff, I. *Science* **2007,** *317*, 100-102.

15. Yu, Y. F.; Huang, S. Y.; Li, Y. P.; Steinmann, S. N.; Yang, W. T.; Cao, L. Y. *Nano Lett.* **2014,** *14*, 553-558.

16. Wu, Z. Z.; Fang, B. Z.; Bonakdarpour, A.; Sun, A. K.; Wilkinson, D. P.; Wang, D. Z. *Appl. Catal., B* **2012,** *125*, 59-66.

17. Faber, M. S.; Lukowski, M. A.; Ding, Q.; Kaiser, N. S.; Jin, S. *J. Phys. Chem. C* **2014,** *118*, 21347-21356.

18. Wadia, C.; Alivisatos, A. P.; Kammen, D. M. *Environ. Sci. Technol.* **2009,** *43*, 2072-2077.

19. *U.S. Geological Survey: Mineral Commodity Summaries 2012*. 2012.

20. Macpherson, H. A.; Stoldt, C. R. *Acs Nano* **2012,** *6*, 8940-8949.

21. Bai, Y. X.; Yeom, J.; Yang, M.; Cha, S. H.; Sun, K.; Kotov, N. A. *Journal of Physical Chemistry C* **2013,** *117*, 2567-2573.

22. Kirkeminde, A.; Ruzicka, B. A.; Wang, R.; Puna, S.; Zhao, H.; Ren, S. Q. *ACS Appl. Mater. Interfaces* **2012,** *4*, 1174-1177.

23. Kirkeminde, A.; Gingrich, P.; Gong, M. G.; Cui, H. Z.; Ren, S. Q. *Nanotechnology* **2014,** *25*.

24. Ennaoui, A.; Fiechter, S.; Tributsch, H.; Giersig, M.; Vogel, R.; Weller, H. *J. Electrochem. Soc.* **1992,** *139*, 2514-2518.

25. Chatzitheodorou, G.; Fiechter, S.; Konenkamp, R.; Kunst, M.; Jaegermann, W.; Tributsch, H. *Mater. Res. Bull.* **1986,** *21*, 1481-1487.

26. Aricò, A. S.; Antonucci, V.; Antonucci, P. L.; Modica, E.; Ferrara, S.; Giordano, N. *Mater. Lett.* **1992,** *13*, 12-17.

27. Rosso, K. M.; Becker, U.; Hochella, M. F. *Am. Mineral.* **1999,** *84*, 1535-1548.

28. Vogt, H.; Chattopadhyay, T.; Stolz, H. J. *J. Phys. Chem. Solids* **1983,** *44*, 869-873.

29. Lutz, H. D.; Muller, B. *Phys. Chem. Miner.* **1991,** *18*, 265-268.

30. Bard, A.; Faulkner, L., *Electrochemical Methods: Fundamentals and Applications*. John Wiley & Sons, Inc: 2001.

31. Leonard, K. C.; Bard, A. J. *J. Am. Chem. Soc.* **2013,** *135*, 15890-15896.

32. Bard, A. J.; Fan, F. R. F.; Pierce, D. T.; Unwin, P. R.; Wipf, D. O.; Zhou, F. M. *Science* **1991,** *254*, 68-74.,

33. Sun, T.; Yu, Y.; Zacher B. J.; Mirkin, M. V. *Angewandte Chemie-International Edition* **2014,** *53*, 14120-14123.

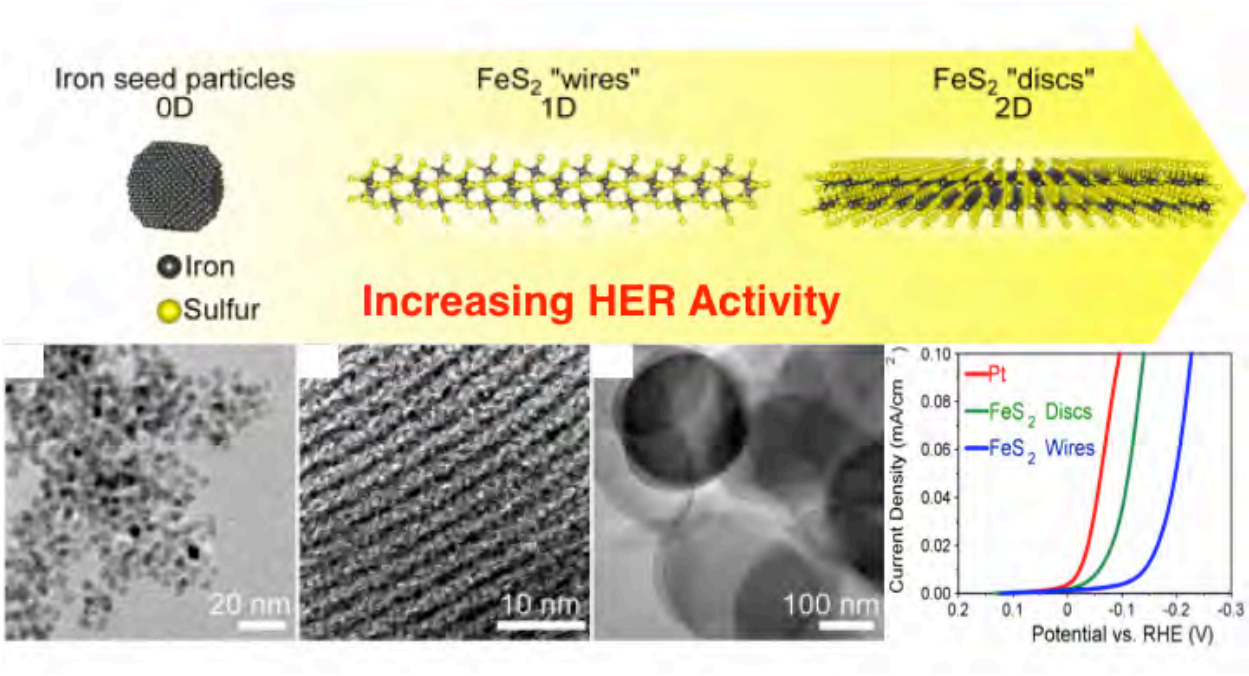

Insert Table of Contents Graphic and Synopsis Here.